Nanoscale

PAPER

View Article Online
View Journal

Check for updates

Cite this: DOI: 10.1039/d5nr04827c

# A mild colloidal strategy for controlling the morphology of reduced graphene oxide–Ag nanowire hybrids

Alessio Massaro,†‡[a] Rafique Ahmed Lakho,[a,b] Adriana Grandolfo,[a,c,d] Giuseppe Valerio Bianco,[e] Elisabetta Fanizza,[a,d,f] Marinella Striccoli,[d,f] Roberto Comparelli,[d,f] Maria Lucia Curri*[a,d,f] and Chiara Ingrosso*[d,f]

A novel hybrid nanocomposite has been synthesized *via* a polyol-based proceed, consisting of polyvinylpyrrolidone (PVP) coated silver nanowires (Ag NWs) decorating Reduced Graphene Oxide (RGO) sheets, functionalized with histidine (His). While conventional methods involve mixing pre-synthesized Ag NWs with graphene derivatives, an approach that typically results in a weak electron coupling between the components, this study presents an *in situ* synthesis strategy designed to promote a stronger interfacial interaction and, hence, electronic connectivity within the nanocomposite. In this nanocomposite, the Ag NWs are coordinated by His molecules, which are non covalently anchored to the RGO basal plane through aromatic π–π stacking interactions. His has been purposefully selected due to its multifunctional role: it facilitates the liquid-phase exfoliation of RGO in water, enables stable dispersion in ethylene glycol, which is an environmentally friendly solvent serving as the reducing agent in the polyol reaction, and acts as a molecular linker between the Ag NWs and the RGO surface. The influence of various experimental parameters on the morphology and size distribution of the Ag NWs across the His-RGO scaffold has been thoroughly explored through spectroscopy and microscopy techniques, enabling a deeper understanding of the nanocomposite's formation mechanism. The findings have revealed that the Ag NWs grow *in situ* on the His-RGO sheets, originating from pre-synthesized AgCl nanocubes that anchor selectively at the coordinating sites of His. Notably, well dispersed His-RGO flakes decorated with morphologically controlled Ag NWs have been successfully obtained in ethanol suspension. These nanostructures can hold significant promise as functional materials for diverse applications, including electrochemical and Surface-Enhanced Raman Spectroscopy (SERS) sensors, temperature sensors, antimicrobial coatings, and thermal management technologies.

Received 14th November 2025,
Accepted 12th February 2026

DOI: 10.1039/d5nr04827c

rsc.li/nanoscale

Open Access Article. Published on 18 February 2026. Downloaded on 3/17/2026 3:37:48 PM.
This article is licensed under a Creative Commons Attribution-NonCommercial 3.0 Unported Licence.

## Introduction

The burgeoning interest in hybrid nanocomposites combining graphene-based materials with colloidal inorganic nanoparticles (NPs) stems from the synergistic integration of their distinct functionalities. This convergence leads to nanostructures with enhanced or entirely new properties, making them attractive for diverse applications, including electronic circuits, (bio)sensors, electro- and photo-catalysis, antimicrobial coatings, and biomedicine.[1–4]

Among graphene derivatives, reduced graphene oxide (RGO) is particularly noteworthy. It retains many of the graphene's exceptional structural and functional characteristics, such as atomic-scale thickness, high optical transparency in the visible spectral range, mechanical flexibility, and excellent in-plane electrical and thermal conductivity, while offering greater chemical versatility.[5] In parallel, colloidal inorganic

[a]*Department of Chemistry, Università degli Studi di Bari, via Orabona 4, 70126 Bari, Italy*
[b]*Department of Aerospace Science and Engineering, Polytechnic of Bari, via Orabona 4, 70126 Bari, Italy*
[c]*Department of Electrical and Information Engineering, Polytechnic of Bari, via Orabona 4, 70126 Bari, Italy*
[d]*CNR-IPCF S.S. Bari, c/o Department of Chemistry, Università degli Studi di Bari, via Orabona 4, 70126 Bari, Italy. E-mail: c.ingrosso@ba.ipcf.cnr.it, marialucia.curri@uniba.it*
[e]*CNR-NANOTEC Sez. Bari, c/o Department of Chemistry, Università degli Studi di Bari, Via Orabona 4, 70126 Bari, Italy*
[f]*Consorzio Interuniversitario Nazionale per la Scienza e Tecnologia dei Materiali (INSTM), Via G. Giusti, 9 50121 Firenze, Italy*
†Present address: Ghent University, Belgium.
‡Present address: Vlaamse Instelling voor Technologisch Onderzoek (VITO), Boeretang 200, 2400 Mol, Belgium.

Open Access Article. Published on 18 February 2026. Downloaded on 3/17/2026 3:37:48 PM.
This article is licensed under a Creative Commons Attribution-NonCommercial 3.0 Unported Licence.

NPs exhibit morphology and phase dependent physical and chemical properties, along with tuneable surface reactivity, which can be precisely tailored using various chemical strategies.[6]

The high surface area and chemical reactivity of RGO make it an ideal platform for the fabrication of hybrid nanocomposites with inorganic nanostructures, through various decoration methods.[7,8] Among the numerous inorganic components explored for integration with RGO, silver nanowires (Ag NWs) have gained considerable attention. Their high electrical and thermal conductivity, mechanical flexibility, optical transparency, plasmonic behaviour and antimicrobial activity make them suitable for applications such as Surface Enhanced Raman Scattering (SERS), pressure and temperature sensors, capacitors, transparent heaters, and transparent electrodes of solar cells and touch panels.[9–13]

When Ag NWs are combined with RGO, they benefit from its dual role as a physical support and protective barrier, which helps prevent NW aggregation and oxidation. This synergy enhances the performance and stability of the resulting hybrid materials, which show great promise for use in flexible and transparent electrodes, electromagnetic interference shielding, SERS platforms, thermal management systems, and antimicrobial coatings.[14–17] Despite this potential, most studies in literature report hybrid nanocomposites prepared by simply mixing pre-synthesized Ag NWs with graphene derivatives.[16] This strategy often leads to a weak electron coupling at the interface, limiting the full exploitation of the constituent materials' properties. This shortcoming is largely attributed to the complexity of the Ag NWs synthesis, which is highly sensitive to factors affecting anisotropic growth and the wire-to-particle yield.

Reports on the *in situ* synthesis of Ag NWs directly on RGO are relatively scarce. In particular, the polyol approach – despite being well-known for its ability to control Ag NWs morphology and yield – has not been extensively applied in the context of *in situ* NWs growth on graphene derivatives. Most existing studies employ solvothermal methods, in which graphene oxide and the Ag precursor are dispersed in a mixture containing polyvinylpyrrolidone (PVP) as a stabilizing agent and ethylene glycol (EG), which serves as both the reductant and the solvent.[15,16] However, these studies often lack mechanistic insights into the growth process of the Ag NWs on the RGO basal plane.

In this study, we present a novel hybrid nanocomposite composed of histidine-functionalized RGO (His-RGO) sheets decorated with Ag NWs, synthesized *via* a modified polyol method.[18] The nanocomposite is obtained by injecting His-RGO into a polyol reaction medium, where Ag NWs are formed directly on the RGO surface through the reduction of silver nitrate ($AgNO_3$) in presence of PVP and NaCl salt.

His is employed as a molecular linker due to its functionalities: it coordinates the surface of Ag NWs and simultaneously anchors to RGO *via* aromatic π–π stacking interactions,[3,4,19] allowing electron coupling between the nanocomposite components.[3] This approach avoids introducing defects into the RGO structure that could compromise its conductivity. Additionally, the water solubility of His facilitates exfoliation and dispersion of RGO in aqueous media, eliminating the need for toxic, high-boiling organic solvents, which are commonly used for exfoliation.[20]

A comprehensive investigation of the synthesis parameters has been carried out, including the His-RGO injection mode, its dissociation state, reaction time, stirring rate, molecular weight of PVP, PVP : $AgNO_3$ molar ratio, and His-RGO : $AgNO_3$ weight ratio (w/w). These parameters have been systematically varied to understand their effects on the morphology and distribution of the Ag NWs on the His-RGO scaffold. Spectroscopic and microscopic analyses have provided detailed insights into the formation mechanism, highlighting the critical influence of the injection strategy and dissociation state of the His-RGO scaffold on the anisotropic growth and successful anchoring of the Ag NWs. The Ag NWs grow *in situ* from AgCl nanocubes, which are preformed and anchor selectively to the His-RGO platform at the histidine coordination sites. PVP facilitates the anisotropic growth, while also enabling the resulting nanocomposite to remain well-dispersed in polar solvents.

The resulting His-RGO/Ag NWs hybrid nanocomposite exhibits excellent dispersibility and solution-processability, making it suitable for integration into a variety of advanced technologies. These include (bio)sensing platforms, optoelectronic devices, antimicrobial coatings, thermally dissipative coatings, particularly for use in flexible and wearable electronics.

## Results and discussion

### Exfoliation and functionalization of RGO with His

Commercially available Reduced Graphene Oxide (RGO) underwent exfoliation and surface functionalization *via* liquid phase exfoliation in aqueous histidine (His) solutions. The process included sonication, ultracentrifugation to isolate the exfoliated material, and subsequent re-dispersion in water, to remove the excess of His.[21,22] During this treatment His interacted with the RGO basal plane through aromatic π–π stacking interactions.[21,22] The exfoliation was further assisted by the carboxyl groups of His, extending out of the RGO plane, together with its amino groups, that facilitated dispersion of RGO in water and prevented π–π driven re-stacking.[3,4] The resulting His-functionalized RGO (His-RGO) complex exhibits a characteristic absorption peak at 275 nm in the UV-Vis spectrum, corresponding to the π–π* transition of the –C=C– bond in the graphene structure[4] (Fig. 1a). Transmission electron microscopy (TEM) reveals nearly electron-transparent, sheet-like structures, ranging from single layers to few- and multi-layered stacks, with visible wrinkles and folded edges due to mechanical deformations of the RGO sheets[23] (Fig. 1b).

The aromatic π–π stacking of His onto the RGO sheets has been demonstrated by the authors in recent works by XPS and FTIR-ATR investigation.[24,25]


This journal is © The Royal Society of Chemistry 2026

Open Access Article. Published on 18 February 2026. Downloaded on 3/17/2026 3:37:48 PM.
This article is licensed under a Creative Commons Attribution-NonCommercial 3.0 Unported Licence.

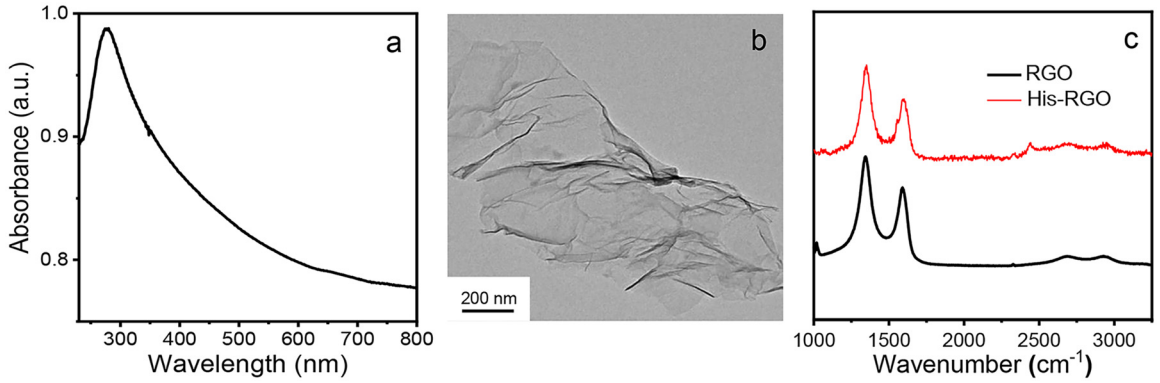


**Fig. 1** (a) UV-Vis absorption spectrum of an aqueous solution of His-RGO. (b) TEM image of His-RGO and (c) Raman spectra of RGO and His-RGO.

Raman spectrum of His-RGO exhibits the typical D and G bands of the pristine RGO at approximately 1349 $cm^{-1}$ and 1582 $cm^{-1}$, respectively (Fig. 1c). The D peak is associated with defects in the carbon lattice and arises from a second-order process involving both inelastic and elastic electron–phonon scattering.[26] The G band, instead, corresponds to the in-plane stretching of C-$sp^2$ bonds within the hexagonal structure.[27] Notably, the positions of the D and G peaks, as well as their intensity ratio, remain unchanged upon His functionalization (Fig. 1c). This observation indicates that the anchoring of His onto RGO does not involve the formation of new $sp^3$ carbon defects,[27] thereby confirming the non covalent nature of the functionalization of RGO, which occurs *via* aromatic π–π stacking interactions.

The ζ-potential of the His-RGO in water at pH 7 results at approximately −20.1 ± 1.5 mV, a negative value attributed to the presence of deprotonated carboxylate groups on His.[19]

## Synthesis and characterization of His-RGO/Ag NWs hybrid nanocomposites

The hybrid nanocomposite of His-RGO decorated with Ag NWs (His-RGO/Ag NWs) was synthesized by modifying the polyol method described by S. Coskun *et al.*[18] In this approach, His-RGO serves as both a structural support and a coordinating site for the silver heteronucleation, owing to the anchoring of His onto the RGO surface.[24] The reaction mixture consisted of His-RGO, polyvinylpyrrolidone (PVP) as both a coordinating and steric stabilizing agent,[18] EG serving as the solvent and reducing agent for $AgNO_3$, and NaCl, to regulate the concentration of $Ag^+$ ions during the synthesis.[28]

In a typical procedure, His-RGO was introduced in a premixed solution of PVP and NaCl in EG, and the system was stirred and heated to 170 °C. A solution of $AgNO_3$ in EG was then added gradually in ten aliquots at 6 min intervals, in order to minimize the risk of $Ag^+$ supersaturation and ensuring the slow NWs formation. To better understand the role of each component in the synthesis, preliminary control experiments were conducted to probe the individual interactions between PVP, EG, $AgNO_3$ and His-RGO. Following this, the main experimental parameters were systematically optimized. The resulting His-RGO/Ag NWs nanocomposites were characterized for their morphology and spectroscopic features and compared with neat Ag NWs synthesized under identical conditions (Fig. S1 of the SI).

## Control experiments

A series of control experiments was conducted to elucidate the individual role of the reagents involved in the synthesis of the His-RGO/Ag NWs hybrid nanocomposite. In general, these tests involved the separate addition of $AgNO_3$, alone or in combination with PVP or EG, into sealed vials containing either His-RGO or pristine RGO, with or without NaCl. Each mixture was stirred at 600 rpm and heated to 170 °C in an oil bath. $AgNO_3$ (2.5 mL of a 20 mg $mL^{-1}$ ethanol solution) was added incrementally in ten aliquots, every 6 min, to achieve a 10 : 1 weight ratio (w/w) of $AgNO_3$ : His-RGO.

## Reactivity of $AgNO_3$ with His-RGO in a non-coordinating solvent

The interaction of $AgNO_3$ with His-RGO in a non-coordinating solvent was tested in the first experiment, designed to probe the reactivity of $AgNO_3$ with His-RGO in absence of the coordinating agent PVP, EG and NaCl. $AgNO_3$ in ethanol was injected into a dispersion of His-RGO in octadecene (ODE), a non-polar, high boiling solvent, not coordinating metal atoms. UV-Vis absorption spectrum of the resulting dispersion reveals a strong RGO absorption signal at 275 nm, and a broad band above 318 nm, likely associated to the localized surface plasmon resonance (LSPR) of polydisperse Ag nanostructures[29] (Fig. 2a, blue line). TEM micrographs confirm the presence of nearly transparent sheet-like His-RGO nanostructures, decorated with high-contrast polydisperse Ag nanoparticles (NPs) (243 ± 242 nm in size) (Fig. 2b and corresponding schematic). A parallel experiment with bare RGO instead of His-RGO produced significantly fewer 160 ± 50 nm sized Ag structures (Fig. 2c and corresponding schematic). This suggests that Ag NPs heteronucleate and grow on His-RGO *via* galvanic reduction with electron transfers occurring from His-RGO to $Ag^+$ ions, a mechanism previously observed in other RGO–metal nanocomposites, where aromatic linkers mediate electron transfer.[3] These findings highlight the key role of His in enabling RGO–Ag electron coupling.[3]

Open Access Article. Published on 18 February 2026. Downloaded on 3/17/2026 3:37:48 PM.
This article is licensed under a Creative Commons Attribution-NonCommercial 3.0 Unported Licence.

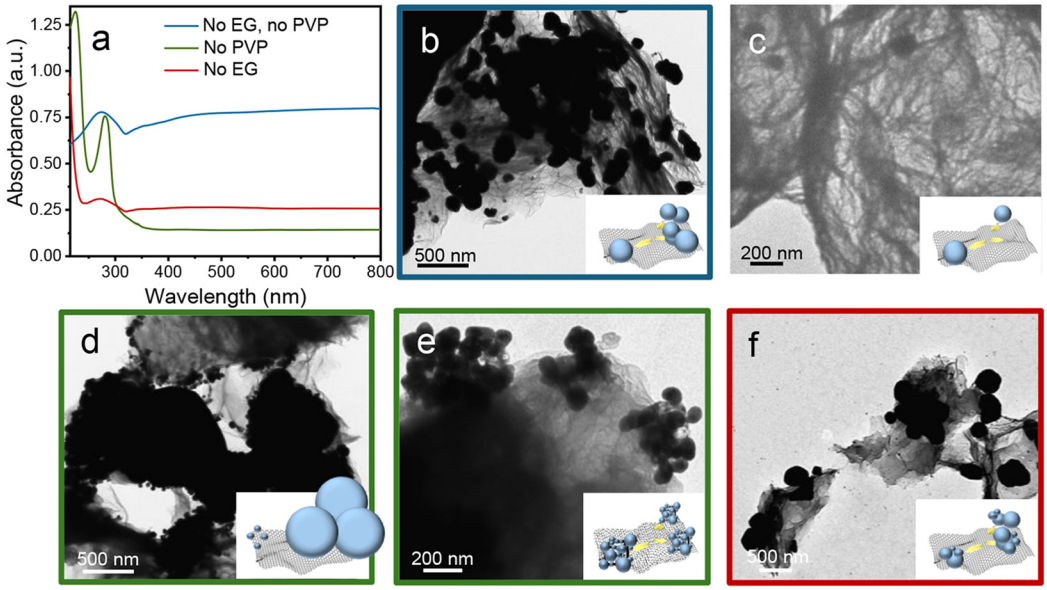


**Fig. 2** (a) UV–Vis absorption spectrum of hybrid nanostructures synthesized at 170 °C for 2.5 h, with stirring rate of 600 rpm, using a 10 : 1 $AgNO_3$ : His-RGO w/w from an ethanol dispersion starting from 4 mg $mL^{-1}$ $AgNO_3$ and 1 mg $mL^{-1}$ His-RGO. (b–f) TEM images of hybrid nanostructures obtained by injecting $AgNO_3$ into different dispersions: (blue line in a and b) His-RGO in ODE, without EG and PVP; (c) RGO in ODE, without EG and PVP; (green line in a, d and e) His-RGO in EG, without PVP; (red line in a and f) His-RGO in ODE, without EG, with PVP ($M_w$ = 360 kDa) at the 7.7 : 1 PVP : $AgNO_3$ molar ratio. The sketches shown as insets in the panels b–f reproduce the morphology of the structures observed in the corresponding TEM images (schematics are not drawn to scale).

### Reactivity of $AgNO_3$ with His-RGO in EG/NaCl, in absence of PVP

The reactivity $AgNO_3$ with His-RGO in EG/NaCl, in absence of PVP was systematically investigated. A solution of $AgNO_3$ in EG was injected into a dispersion of His-RGO and NaCl in EG. The resulting UV-Vis absorption spectrum exhibits peaks at 225 nm and 281 nm, characteristic of AgCl NPs,[30] arising from the reaction between $Ag^+$ and $Cl^-$, along with a weak LSPR peak of Ag at 431 nm (Fig. 2a, green line). TEM analysis reveals the presence of high-contrast micrometre-sized Ag structures together with smaller Ag NPs (Fig. 2d and corresponding schematic), as well as nodule-like nanostructures anchored to the His-RGO sheets (Fig. 2e and corresponding schematic).

These morphologies closely resemble those reported for AgCl nanocubes by M. W. Schuette *et al.*[28] identified by XRD during the polyol synthesis of Ag NWs in the presence of NaCl. The surface of such nanocubes serve as preferential site for the heteronucleation of Ag NPs *via* the reduction of $Ag^+$ by EG, which is oxidized to glycolaldehyde during the process.[31] Consistently, similar nodular structures were also observed in aliquots collected from the reference Ag NWs synthesis after six injections of $AgNO_3$ (Fig. S1a).

### Reactivity of $AgNO_3$ with His-RGO in presence of PVP, without EG

$AgNO_3$ reactivity with His-RGO in presence of PVP, without EG, was assessed by injecting $AgNO_3$ in ethanol into a dispersion of PVP and His-RGO in ODE. The UV-Vis spectrum again shows the characteristic RGO absorption peak at 275 nm, together with a broad band extending above 321 nm (Fig. 2a, red line), which can be attributed to the LSPR of polydisperse Ag nanostructures.[29] Consistent with this assignment, TEM analysis reveals Ag nanostructures and aggregates heteronucleated on the His-RGO surface, with a mean size of 208 ± 138 nm (Fig. 2f and corresponding schematic). These structures are noticeable smaller and more uniform than those obtained in the absence of PVP (Fig. 2b and d), clearly indicating that PVP plays a key role in regulating the morphology of the Ag NPs.

Taken together, these control experiments demonstrate that, in the presence of His-RGO and NaCl, AgCl nanocubes initially formed. Remarkably, these nanocubes preferentially anchor to the nitrogen and carboxylate groups of His on the RGO surface (Fig. 3), in agreement with previous XPS evidence of Ag nanostructures heteronucleated on His-RGO sheets.[24] At the surface of the AgCl nanocubes, Ag atoms subsequently heteronucleate into NPs, forming the observed nodule-like structures (Fig. 2e).[28] Importantly, similar nodule-like structures were also observed during the synthesis of the reference Ag NWs sample, where Ag nanofilaments were found to grow from the nodules after the seventh $AgNO_3$ injection (Fig. S1b), consistently with earlier reports by S. Coskun *et al.*[18] and M.W. Schuette *et al.*[28] These observations strongly suggest that the nodules anchored to the His-RGO surface likely serve as nucleation centres for the subsequent anisotropic growth of Ag NWs, with PVP acting as the morphology directing agent.[28]

Interestingly, this study proposes for the first time, to the best of our knowledge, that Ag NWs growth may initiate from Ag nodules anchored to the His-RGO platform.

Open Access Article. Published on 18 February 2026. Downloaded on 3/17/2026 3:37:48 PM.
This article is licensed under a Creative Commons Attribution-NonCommercial 3.0 Unported Licence.

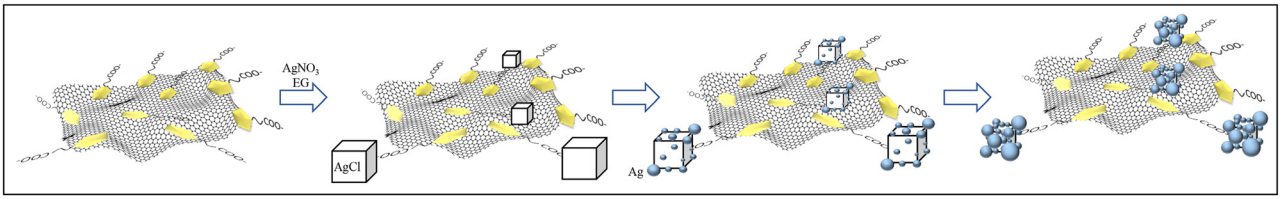


**Fig. 3** Proposed mechanism for the formation of nodule-like structures on the His-RGO sheets (schematics are not drawn to scale).

To validate this mechanistic understanding and develop a reproducible, solution-processable synthesis method suitable for the His-RGO/Ag NW hybrid nanocomposite, we introduced His-RGO into a reaction mixture containing EG, $AgNO_3$, NaCl, and PVP. We then systematically investigated key experimental parameters known to affect NW growth and properties, including reaction time, PVP molecular weight and concentration, PVP : $AgNO_3$ molar ratio,[18] injection mode and dissociation state of the His-RGO complex, and $AgNO_3$ : His-RGO w/w.

### Injection strategy for His-RGO in the synthesis mixture

The injection mode of His-RGO into the Ag NWs synthesis mixture was systematically investigated to minimize interference of the His coordination sites with the anisotropic growth of the NWs, that is promoted by PVP.[28] Injection of His-RGO was performed in three different conditions: i. since the beginning of the synthesis process, mixing His-RGO with $AgNO_3$, PVP, NaCl in EG, ii. after the complete injection of $AgNO_3$, and iii. after the seventh injection of $AgNO_3$ in the synthesis solution. The experiments were conducted using PVP with a $M_w$ of 360 kDa, maintaining a fixed PVP : $AgNO_3$ molar ratio of 7.7 : 1 and an $AgNO_3$ : His-RGO w/w of 10 : 1. The synthesis was carried out at 170 °C with a stirring rate of 600 rpm.

In the initial approach, His-RGO powder was dispersed in a solution of PVP and NaCl in EG, and the $AgNO_3$ solution (20 mg $mL^{-1}$ in EG) was added incrementally in 2.5 mL portions every 6 min. As $AgNO_3$ was introduced, the dispersion changed colour: initially black, it turned light grey after the first addition, consistent with the formation of milky white AgCl.[18,28] Between the second and sixth $AgNO_3$ injections, the characteristic colour transition from bright to dark orange, commonly observed during Ag NWs synthesis,[18] was not visible, likely masked by the inherent dark colouration of His-RGO. After the seventh injection, however, the solution turned dark silver shade, indicating the onset of the Ag NWs growth.[18] The corresponding UV-Vis absorption spectrum exhibits a prominent RGO peak at 275 nm and a broad LSPR band extending above 315 nm, with distinct features at 340 and 410 nm (Fig. 4a, blue line). TEM analysis confirms the formation of elongated nanostructures, with an average length of 4 ± 2 μm and a diameter of 200 ± 100 nm heteronucleated onto the His-RGO sheets (red arrow in Fig. 4b and corresponding schematic). These structures are reasonably ascribed to Ag NWs based on their distinguishable image contrast (Fig. S1c), along with micrometre-sized Ag particles (brown arrow in Fig. 4b and corresponding schematic), as well as spherical nanoparticles and irregular Ag nanostructures (yellow arrow in Fig. 4c) are also observed. Notably, the Ag NWs formed in the presence of His-RGO are shorter and thicker than those obtained in the reference synthesis (8 ± 3 μm in length and 70 ± 20 nm in diameter; Fig. S1c). This morphological evidence enables a clear assignment of the features observed in the UV-Vis spectrum (Fig. 4a, blue line). The absorption peak at 340 nm is attributed to the quadruple resonance of the Ag NWs[32] and is blue-shifted relative to the corresponding feature in the control sample at 349 nm (Fig. S1d). Conversely, the transverse plasmon resonance peak at 410 nm is red-shifted compared to the control (381 nm) (Fig. S1d), in agreement with the increased NW diameter (200 ± 100 nm *vs.* 70 ± 20 nm in the reference Ag NWs[32]). Furthermore, the broadened LSPR band and elevated baseline (Fig. 4a, blue line) confirm the presence of polydisperse Ag nanostructures[29] and enhanced light scattering from micrometre-scale Ag particles and multilayer His-RGO sheets. Although a distinct AgCl spectral signature is not detected at the reaction time of 2.5 h (Fig. 4a), both literature reports,[18,28] and the control experiments (Fig. 2a) support the intermediate formation of AgCl nanocubes.

Additional TEM observations reveal Ag NPs surrounded by a low-contrast layer, attributed to PVP, in close proximity to Ag nanostructures anchored to the His-RGO sheets (green arrows in Fig. 4d and corresponding schematic). Notably, Fig. 4e shows two NWs emerging from a single Ag nodule, anchored to the His-RGO surface (blue arrows in Fig. 4e and corresponding schematic), suggesting a unique previously unreported growth pathway.

The effective heteronucleation of both nodules and Ag NWs on the His-RGO sheets is further supported by low-magnification TEM images, which clearly show a preferential localization of these structures on the His-RGO platform (Fig. S2), consistent with coordination at His functional groups, as previously demonstrated by XPS analysis.[24]

To reduce the formation of undesired byproducts, His-RGO was instead introduced only after completing the $AgNO_3$ injections. The dispersion was added to the synthesis mixture preheated to 170 °C, to promote surface anchoring of His-RGO during the dynamic PVP absorption/desorption on growing Ag NWs. The UV-Vis spectrum of this sample shows the RGO peak at 275 nm, a shoulder at 355 nm, the quadrupole resonance, and a transverse plasmon peak[32] at 400 nm (Fig. 4a, green line). TEM images show mostly bare His-RGO sheets and polydisperse, homonucleated NWs (length: 5 ± 3 μm, dia-

Open Access Article. Published on 18 February 2026. Downloaded on 3/17/2026 3:37:48 PM.
This article is licensed under a Creative Commons Attribution-NonCommercial 3.0 Unported Licence.

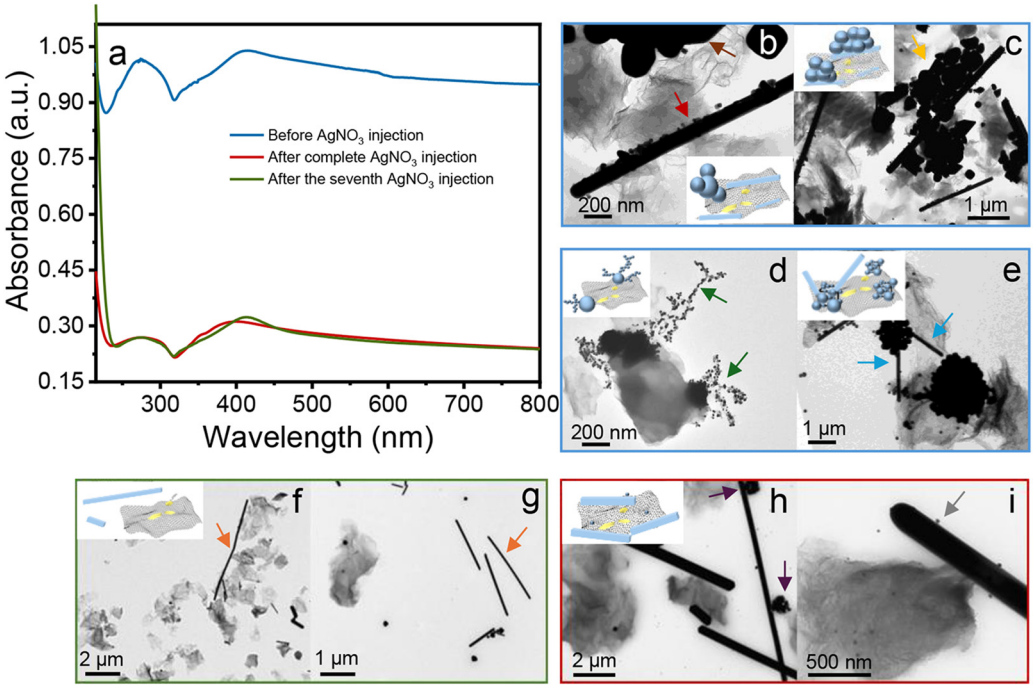


**Fig. 4** (a) UV-Vis absorption spectra and (b–i) TEM images of hybrid nanostructures synthesized with the 10 : 1 $AgNO_3$ : His-RGO w/w, 7.7 : 1 PVP : $AgNO_3$ molar ratio, at 170 °C, reaction time of 2.5 h, PVP at $M_w$ of 360 kDa, stirring rate of 600 rpm, by injecting His-RGO (blue line in a, b–e) in the synthesis solution containing PVP and NaCl, then added by $AgNO_3$, (green line in a, f and g) after complete injection of $AgNO_3$, and (red line in a, h and i) between the seventh and eighth injection of $AgNO_3$. The spectra in (a) were recorded from ethanol dispersions starting from 4 mg $mL^{-1}$ $AgNO_3$ and 1 mg $mL^{-1}$ His-RGO. The arrows indicate the relevant structures commented in the text. Insets in panels b–f and h show schematics reproducing the corresponding TEM morphologies (schematics are not drawn to scale).

meter: 110 ± 6 nm), along with spherical Ag NPs (orange arrows in Fig. 4f and g and sketch of panel f), indicating limited interactions between His-RGO and the NWs due to steric hindrance.

To enhance heteronucleation, His-RGO was instead added after the seventh Ag precursor injection, when Ag NWs growth had already started,[18] *via* a pre-heated (170 °C) EG dispersion.

TEM analysis of the resulting nanocomposite shows polydisperse NWs (average length: 6 ± 5 µm, diameter: 270 ± 100 nm) heteronucleated on His-RGO, Ag nodules (purple arrows in Fig. 4h) and spherical Ag NPs (39 ± 12 nm) at the Ag NWs surface (grey arrows in Fig. 4i and sketch of panel 4h), along with homonucleated Ag NWs (data not shown). The UV-Vis spectrum (Fig. 4a, red line) shows the RGO peak at 275 nm and the shoulder of the quadrupolar resonance of the Ag NWs at 330 nm, with the transverse plasmon peak at 413 nm.[32] The predominance of NWs heteronucleated on His-RGO (Fig. 4h and i) with respect to byproducts, validates this injection timing for subsequent studies. Then, to ensure the full transformation of the Ag nodules into NWs, the reaction time was extended.

### Influence of reaction time and related parameters on NW growth

To evaluate the impact of the reaction time on the Ag NWs formation, the synthesis was extended first to 5 h and then to 6.5 h, while all the other experimental conditions were kept constant. After 5 h, the UV-Vis absorption spectrum of the nanocomposite shows the characteristic RGO peak at 275 nm and a pronounced broad LSPR band above 319 nm (Fig. 5a), with significantly greater intensity than that observed for the sample collected after 2.5 h of synthesis (Fig. 4a, again shown in Fig. 5a, green line). Two additional shoulders appeared at 354 nm and 392 nm, corresponding to the quadrupole and transverse plasmon resonance modes of the NWs, respectively[32] (Fig. 5a). An increase of the intensity of the baseline signal was also observed, likely due to light scattering form micrometre sized Ag nodules and multilayered His-RGO.

Notably, the transverse plasmon resonance peak exhibited a blue shift (Fig. 5a, blue line) moving from 413 nm in the 2.5 h sample (Fig. 5a, green line) to 392 nm after 5 h, indicating a decrease in the NWs diameter.[32] This was corroborated by TEM images, which showed that the NWs in the sample achieved after 5 h of reaction (figure and sketches of panels 5c and d) were shorter and narrower than those formed after 2.5 h (figure and sketch of panel 5b), with average dimensions of 5.0 ± 3.0 µm in length and 80 ± 21 nm in diameter (Fig. S3), heteronucleated onto His-RGO sheets.

Spherical Ag NPs were also observed (Fig. 5c), with a mean diameter of 143 ± 72 nm, larger than those seen in earlier stage samples (figure and sketch of panel 5b). This increase in Ag NPs mean size is likely related to Ostwald ripening, a


This journal is © The Royal Society of Chemistry 2026

Open Access Article. Published on 18 February 2026. Downloaded on 3/17/2026 3:37:48 PM.
This article is licensed under a Creative Commons Attribution-NonCommercial 3.0 Unported Licence.

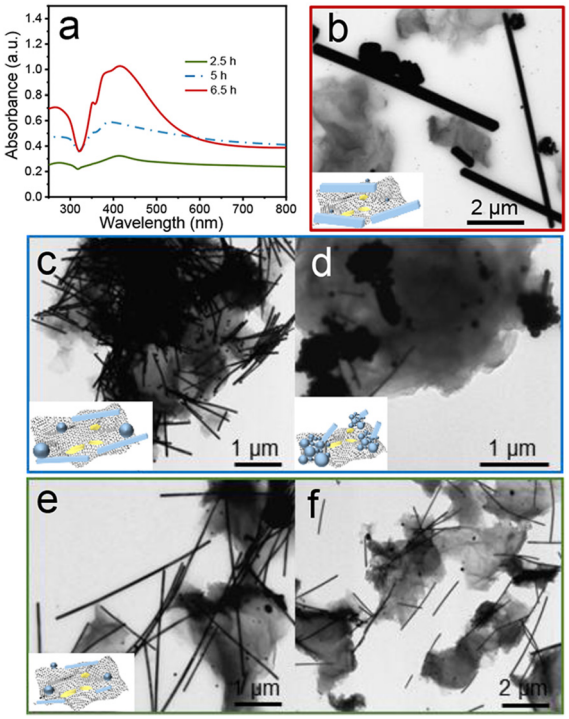


**Fig. 5** (a) UV-Vis absorption spectra and (b–f) TEM images of hybrid nanocomposites synthesized with a 10 : 1 $AgNO_3$ : His-RGO w/w, 7.7 : 1 PVP : $AgNO_3$ molar ratio, PVP of 360 kDa, at 170 °C and 600 rpm stirring rate, with His-RGO injected between the seventh and eighth $AgNO_3$ addition. Reaction times were (b) 2.5 h, (c and d) 5 h and (e and f) 6.5 h. UV-Vis absorption spectra (a) were collected from ethanol dispersions starting from 4 mg $mL^{-1}$ in $AgNO_3$ and 1 mg $mL^{-1}$ in His-RGO (schematics are not drawn to scale).

process in which smaller particle dissolve into $Ag^+$ ions that subsequently redeposit onto larger NPs.[31]

Despite the extended reaction time, TEM images still revealed the presence of Ag nodules with protruding filaments on the His-RGO sheets (figure and sketch of panel 5d), suggesting that the conversion of $Ag^+$ to fully grown NWs was incomplete. Therefore, the reaction time was further increased to 6.5 h, to promote complete $AgNO_3$ conversion in NWs.

At 6.5 h, the UV-Vis absorption spectrum revealed a further increase in intensity of the broad LSPR band of the NWs (Fig. 5a), probably reflecting the reaction of residual $AgNO_3$ precursor, that remained unconverted after 5 h. Since the LSPR band intensity is not strongly dependent on NWs morphology[32] this increase primarily indicates a higher concentration of plasmonic nanostructures. The spectrum displayed distinct peaks at 352 and 378 nm, attributed to the quadrupole and transverse plasmon resonances of the NWs, as well as an LSPR peak at 415 nm corresponding to spherical Ag NPs.[33] The broadening of the LSPR band can be ascribed to light-trapping effects caused by hotspots at the NWs junctions.[34] TEM images showed a dense population of NWs and a significant reduction in both the number and size of the spherical NPs, with an average diameter of 76 ± 44 nm, together with the complete disappearance of nodules (Fig. 5e and f), suggesting that their conversion into NWs reached completion. Concurrently, the presence of a few larger structures with dimensions of several hundred nanometres can also be observed (Fig. 5e).

The resulting NWs exhibited greater monodispersity, with reduced dimensions averaging 2.8 ± 0.8 μm in length and 50 ± 10 nm in diameter (Fig. 5e, f and Fig. S4). The observed shortening and narrowing of the NWs were not attributed to etching effect by $HNO_3$, which can form during $Ag^+$ reduction by EG,[35] because the pH of the solution only slightly decreased, from 5.6 to 4.9 after 5 h of reaction and to 4.7 after 6.5 h.

Six cycles of acetone washing were performed to remove excess PVP from the as-synthesized His-RGO/Ag NWs nanocomposite, thereby enabling its dispersion in ethanol. After purification, the surface morphology of the nanocomposite was preserved, as confirmed by TEM analysis of the purified nanocomposite (Fig. S5a), indicating that the coordination of the Ag NWs to the His-RGO complex is robust and withstands the washing treatment. Additional evidence of the stability of the Ag NWs – His-RGO coordination was obtained by subjecting the purified nanocomposite to an etching procedure using a concentrated ammonia/30% hydrogen peroxide solution (9 : 1 v/v), a treatment reported in literature for the partial removal of PVP from the Ag NWs surface and for increasing their surface roughness. As previously reported, the PVP coating coordinated to the Ag NWs cannot be readily removed by conventional washing procedures.[36] TEM images show that the anchoring of the Ag NWs to the His-RGO surface is preserved even after this more aggressive treatment (Fig. S5b). Raman spectroscopy of the nanocomposite confirmed that the decoration of His-RGO with the Ag NWs did not shift the position of the D and G bands. However, a decrease in the D/G intensity ratio was observed (Fig. S6) indicating enhanced graphitization of residual GO domains within the RGO basal plane, a process induced by EG reduction under the synthesis conditions.[37]

### Influence of His-RGO dissociation, PVP molecular weight, reagent ratios, and stirring rate

The effect of various synthetic parameters on the formation and morphology of the Ag NWs in the hybrid nanocomposite was systematically investigated. A key factor influencing nanostructure formation was the dissociation state of the His-RGO complex, as reflected by its ζ-potential. When His-RGO was isolated from an aqueous solution at pH 11, it exhibited a ζ-potential of −24.5 ± 1.8 mV, indicative of a high degree of carboxyl group deprotonation. As a result, the hybrid nanocomposites formed under these conditions showed elongated nanostructures, approximately 0.6 μm in length and 0.1 μm in diameter (aspect ratio ≈ 6) anchored on the His-RGO sheets (Fig. S7a). These structures resembled nanorods rather than NWs.[38] This deviation is likely due to the high degree of dissociation of carboxylate groups in His at alkaline pH, which enhanced their coordination to the Ag clusters surface and

Open Access Article. Published on 18 February 2026. Downloaded on 3/17/2026 3:37:48 PM.
This article is licensed under a Creative Commons Attribution-NonCommercial 3.0 Unported Licence.

competed with PVP, thereby limiting its ability in guiding anisotropic NWs growth.

Remarkably, the results demonstrated an effective control over the unidirectional growth of the Ag NWs in the nanocomposite when PVP with a high molecular weight (360 kDa) was used at a PVP : $AgNO_3$ molar ratio of 7.7 : 1. Conversely, using lower molecular weight PVP (55 kDa), which is known to promote monodisperse Ag NWs,[18] resulted mainly in spherical Ag NPs and few NWs (~3 ± 1 μm long, ~100 nm diameter, Fig. S7b), with some particles reaching sizes of hundreds of nanometres. Additionally, irregular micrometre-sized Ag aggregates were observed (Fig. S7c), suggesting that lower molecular weight PVP was insufficient to provide the steric stabilization necessary for guiding uniaxial growth.

When the PVP : $AgNO_3$ molar ratio was increased to 11.5 : 1 while maintaining the higher PVP molecular weight (360 kDa), the resulting nanostructures were predominantly composed of spherical Ag NPs, with few NWs measuring 1 μm in length and 50 nm in diameter (Fig. S7d). These findings suggest that excessive PVP coverage led to indiscriminate coordination of all crystal facets, suppressing the anisotropic growth required for NWs formation.[39]

Adjusting the $AgNO_3$ : His-RGO w/w from 10 : 1 to 5 : 1 also impacted nanocomposite morphology. The UV-Vis absorption spectrum (Fig. S8a) exhibited a lower LSPR band intensity and an increase in the baseline absorption, likely due to scattering from stacked His-RGO layers. The transverse plasmon peak was obscured (Fig. S8a), possibly by the broad LSPR of abundant spherical Ag NPs. Although the dimensions of the Ag NWs remained like those in the 10 : 1 w/w sample (Fig. 5e and f), the higher concentration of His-RGO, correlating with increased surface charge, further competed with PVP during the growth. This resulted in many Ag nodules and spherical Ag NPs (Fig. S8b), slowing NWs formation. Prolonging the reaction time to 7.5 h enabled full conversion of nodules into NWs, yielding wires ~2.0 ± 1.0 μm in length and ~100 nm diameter (Fig. S8c).

Stirring rate also played a critical role. At a reduced rate of 200 rpm, the resulting nanocomposite exhibited a weaker LSPR band and red shifted quadrupole and transverse plasmon peaks (Fig. S8d) relative to the sample stirred at 600 rpm (Fig. 5a). TEM analysis revealed longer, thicker NWs, residual spherical NPs and unconverted Ag nodules (Fig. S8e), indicating that slower stirring hindered monomer diffusion and created local concentration gradients.[18] However, extending the reaction time to 7.5 h under slow stirring rate, led to full conversion of the nodules into NWs (~2 μm long and ~40 nm diameter) (Fig. S8f), confirming that reaction kinetics and monomer availability remain key factors in complete NW formation, particularly under constrained mass transport conditions.

Taken together, these results highlight that the dissociation state of His-RGO, quantified *via* ζ-potential, significantly influences coordination dynamics during silver growth. Stronger surface charge enhances competition with PVP for seed surface binding, disrupting the templated NW growth pathway. Optimal balance between ligand coordination, reagent ratios, and reaction dynamics is thus critical to achieve controlled NW synthesis.

### Reaction mechanism of His-RGO/Ag NWs formation

The formation mechanism of His-RGO/Ag NWs was investigated by monitoring the progression of the synthesis through sequential withdrawal of aliquots of the solution after each $AgNO_3$ injection, both before and after the addition of His-RGO. Each aliquot was purified by centrifugation in acetone and subsequent re-dispersion in ethanol and analysed for its spectroscopic and morphological characteristics.

Upon the first $AgNO_3$ injection into a solution of PVP and NaCl in EG, the reaction mixture turned milky white, indicating the formation of AgCl nanocubes,[18,28] (Fig. 6a, photograph I). Following the second injection, the mixture developed a pale orange hue (photograph II), which deepened after the subsequent IV and VI injections (photographs IV and VI). Corresponding UV-Vis absorption spectra of the second and fourth aliquots revealed broad plasmon absorption bands across the visible spectral region (Fig. 6b, traces II and IV), consistent with polydisperse Ag nanostructures.[29] TEM images confirmed the presence of AgCl nanocubes coated with Ag nodules (Fig. 6c, images II and IV), along with some spherical Ag NPs (~19 nm) (data not shown). These features persisted through the fifth injection, with increased Ag NPs concentration (data not shown).

After the sixth $AgNO_3$ addition, the solution turned dark orange (Fig. 6a, photograph VI), and the UV-Vis spectrum exhibited a narrower, blue shifted plasmon peak, centred around 400 nm (Fig. 6b, trace VI), consistent with TEM showing the predominance of smaller ~7 nm spherical Ag NPs, and continued presence of Ag nodules (Fig. 6c, image VI).

Additionally, strong absorption between 240 and 300 nm likely arose from overlapping contribution of the PVP : $Ag^+$ complex[40] (Fig. 6b) and the AgCl direct bandgap transition.[30]

Upon the seventh $AgNO_3$ injection, the reaction mixture turned grey and darkened further after His-RGO addition (Fig. 6a photograph VII) coinciding with significant spectral changes. A broad plasmon band emerged, featuring quadrupolar and transverse plasmon resonance of Ag NWs at 350 nm and 380 nm, respectively, as well as a peak at 430 nm attributable to spherical Ag NPs (Fig. 6b, trace VII). These spectral features persisted through the tenth injection (Fig. 6b, traces VII–X).

After His-RGO was introduced, NWs appeared heteronucleated on the His-RGO sheets, accompanied by additional homonucleated Ag NWs and spherical Ag NPs of *ca.* 36 nm (Fig. 6c, image VII). This confirms that filament growth began *in situ* from nodules interacting with His-RGO, consistent with observations in Fig. 5d.

Subsequent aliquots (ninth and tenth injections) showed continued elongation of Ag NWs, both anchored to His-RGO and suspended in solution, along with spherical Ag NPs growing to ~50 nm (Fig. 6c, images IX and X).


This journal is © The Royal Society of Chemistry 2026

Open Access Article. Published on 18 February 2026. Downloaded on 3/17/2026 3:37:48 PM.
This article is licensed under a Creative Commons Attribution-NonCommercial 3.0 Unported Licence.

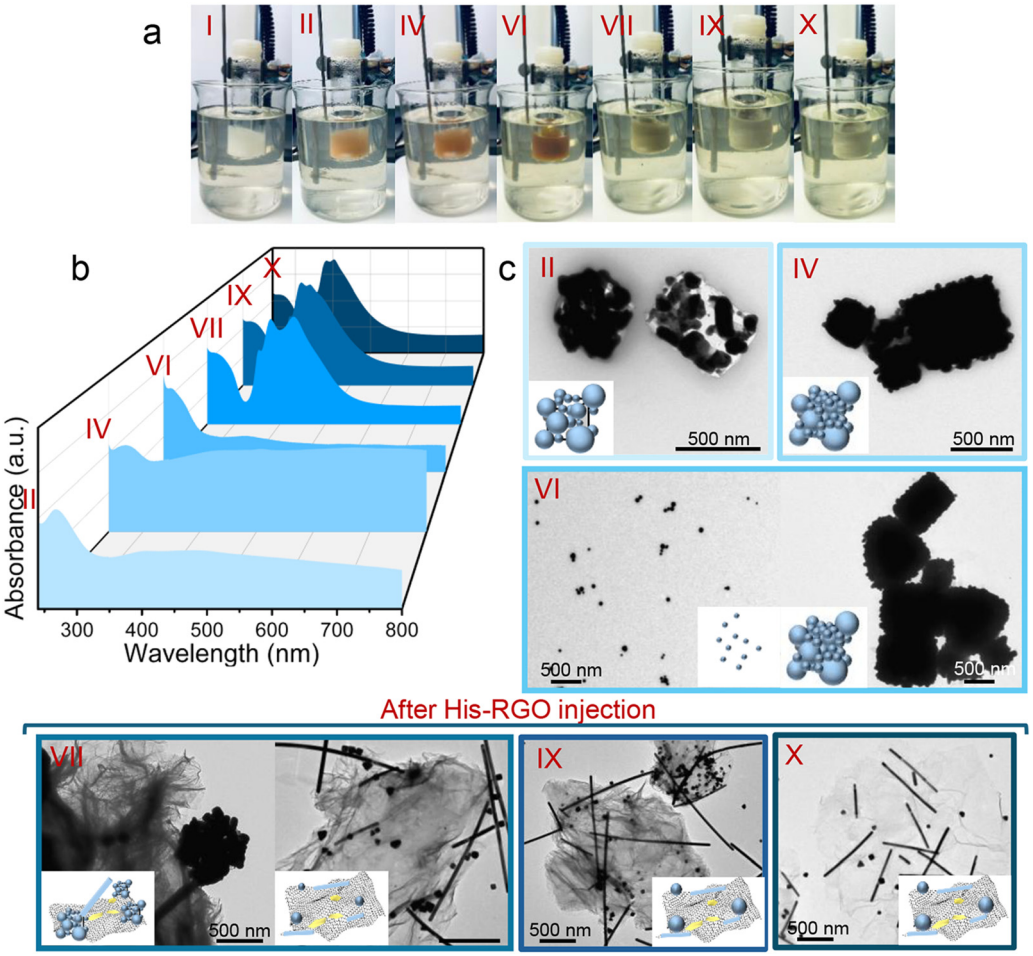


**Fig. 6** (a) Photographs of the synthesis mixture and (b) UV-Vis absorption spectra and (c) TEM micrographs of the aliquots withdrawn from the synthesis solution soon after the first (I), second (II), fourth (IV), sixth (VI), seventh (VII), ninth (IX) and tenth (X) $AgNO_3$ injection. His-RGO was added between the VII and the VIII injection of $AgNO_3$. The synthesis was performed with the 10 : 1 $AgNO_3$ : His-RGO w/w, 7.7 : 1 PVP : $AgNO_3$ molar ratio, at 170 °C, PVP 360 kDa, stirring rate of 600 rpm, reaction time of 6.5 h. Absorption spectra have been registered in ethanol and normalized at the characteristic absorption peak of the PVP : Ag(I) complex at 270 nm (ref. 40) (schematics are not drawn to scale).

The growth of metal nanowires has been widely attributed in the literature to anisotropic confinement, provided by physical templates and surface-capping reagents.[41] Various surfactants have been investigated to kinetically control the growth rates of metal nanoparticles and achieve one-dimensional (1D) growth[41] Wang *et al.* have demonstrated the synthesis of Au nanorods using cetyltrimethylammonium bromide (CTAB) and tetraoctylammonium bromide (TOAB) as capping reagents.[42] The same approach has been used by M. A. El-Sayed *et al.* to generate Au nanorods controlling their aspect ratios,[43] and by Murphy *et al.* for the synthesis of Au and Ag nanorods with relatively high aspect ratios.[44]

In general, the 1D nanostructures grown in the presence of CTAB as the capping reagent exhibit twinned crystal structures. Based on electron diffraction and high-resolution transmission electron microscopy (HRTEM) analyses, Mann *et al.*[45] and Gai *et al.*[46] have proposed a mechanism in which Au nanorods evolve from multiply twinned particles (MTPs) with a decahedral geometry.

Within this framework and building on the earlier work of P. Y. Silvert *et al.*[47] on the polyol synthesis of Ag colloids, which addressed the formation of decahedral MTPs, as well as on the studies by M. W. Schuette *et al.*[28] and Y. Sun *et al.*[41] where NWs evolve from decahedral multiply twinned particles under control of PVP, an analogous growth mechanism can be envisioned. Based on our observations, the growth of Ag NWs likely proceeds *via* MTP intermediates, with PVP playing a key role in directing anisotropic growth, as illustrated schematically in Fig. 7.

1. *AgCl nanocube formation*: after the first $AgNO_3$ injection, as previously demonstrated by M. W. Schuette *et al.* for the synthesis of neat Ag NWs,[28] AgCl nanocubes form and precipitate, due to their lower solubility compared to $AgNO_3$ [48] (Fig. 7, step I). These cubes slowly release $Ag^+$, buffering the $Ag^+$ concentration and limiting spontaneous nucleation.[28]

2. *Nodule formation*: at the second injection of $AgNO_3$, the Ag atom concentration exceeds the supersaturation threshold[49] leading to the homonucleation of Ag NPs and heteronuclea-

Open Access Article. Published on 18 February 2026. Downloaded on 3/17/2026 3:37:48 PM.
This article is licensed under a Creative Commons Attribution-NonCommercial 3.0 Unported Licence.

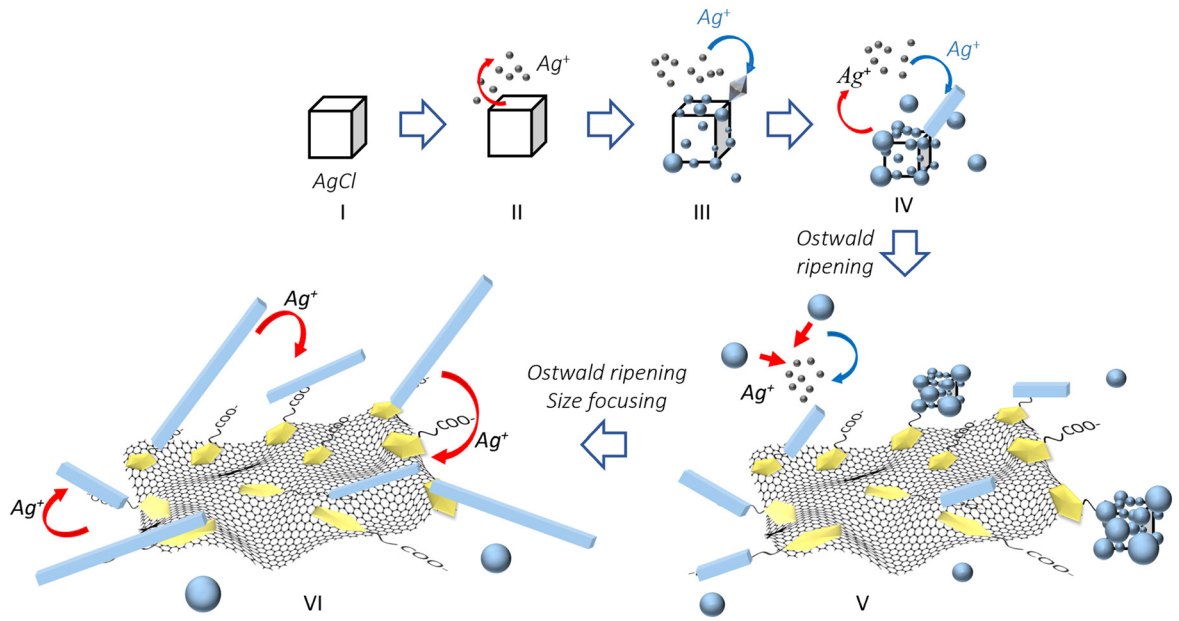


**Fig. 7** Schematic representation of the synthesis reaction mechanism (not to scale).

tion of Ag nodules on AgCl nanocubes (Fig. 7, step II), as previously addressed by W. M. Schuette *et al.*[28] These species are sterically stabilized with PVP.

3. *Nodule growth*: continued Ag precursor additions (up to the fifth injection) result in the constant-size spherical Ag NPs (*ca.* 19 nm) and the gradual growth of the Ag nodules *via* Ag monomers deposition on the AgCl nanocube surface (Fig. 7, steps II and III).

4. *Seeds formation*: after the sixth injection, the concentration of the Ag NPs increased, while their size significantly decreased.

At this stage, similarly to what reported by W. M. Schuette *et al.*[28] and Y. Sun *et al.*[41] in the synthesis of neat Ag NWs, it could be inferred that, under thermodynamically controlled conditions, the low concentration of Ag atom monomers in solution promotes, onto the surface of the AgCl nanocubes, the heteronucleation of the multiply twinned Ag particles. These seeds (Fig. 7, step III) serve as the precursors to the anisotropic NWs growth (Fig. 7, step IV).[28] In terms of surface-energy minimization, the formation of such twinned Ag seeds is favourable once the particle size reaches a critical value.[50]

5. *Nucleation of the NWs*: as demonstrated by Y. Sun *et al.*,[41] the multiply twinned Ag seeds adopt a decahedral topology, characterized by twin boundaries distributed according to a fivefold symmetry. Owing to their high surface energy, twin boundaries act as preferential sites that attract Ag atoms diffusing from the solution. The crystallization of Ag atoms on the twin boundaries initiates the uniaxial elongation of the seeds into the rod-shaped nanostructures and NWs[41] (Step IV). The high reaction temperature (170 °C) accelerates the oxidation of EG to glycolaldehyde,[31] enhancing reaction kinetics and favours the conversion of Ag nodules in the more thermodynamically stable pentagonal twinned prisms.[18] Literature supports Ag NWs formation at 110°–200 °C with faster kinetics at higher temperatures. At 110 °C, the NWs have been reported to form only at long reaction times (12 h),[51] while at higher temperatures their synthesis is significantly faster, typically occurring within few hours.[35] In this study, a reaction temperature of 170 °C was selected, as it has previously shown to yield neat Ag NWs efficiently in just 1.5 h.18 Maintaining a constant concentration of $AgNO_3$, further increases in temperature would likely enhance the formation of pentagonal twinned seeds, ultimately resulting in Ag NWs with lower aspect ratio.[18]

6. *Growth of the NWs*: the twinned Ag seeds exhibit a face-centred cubic (FCC) structure. The {111} planes are denser in atoms and twin boundaries than the {100} facets and hence possess higher surface energy.[52,53] PVP preferentially coordinates with the {100} planes, restraining their growth and promoting unidirectional elongation along the {111} planes. The anisotropic growth is thermodynamically controlled by (i) the slow release of $Ag^+$ ions in solution, which keeps low the Ag atom monomers concentration, and (ii) the selective binding of PVP to the {100} facets. At the end of the synthesis, PVP remains coordinated to the Ag NWs' surface (Fig. S9), enabling their dispersion in polar solvents.

The proposed mechanism, AgCl nanocubes → nodules → pentagonal twins → NWs, is further supported by TEM images of Ag NWs heteronucleated onto the His-RGO platform, exhibiting ends with a rounded, pyramidal profile (Fig. S10), the same morphology as that observed in the work of Y. Sun *et al.*[41] This morphology can be rationalized by a pentagonally twinned growth mechanism, in which anisotropic Ag deposition is favored at the {111} facets of multiply twinned seeds —corresponding to the nanowire ends—while growth at the {100} facets is hindered by the stronger interaction with PVP.


This journal is © The Royal Society of Chemistry 2026

Open Access Article. Published on 18 February 2026. Downloaded on 3/17/2026 3:37:48 PM.
This article is licensed under a Creative Commons Attribution-NonCommercial 3.0 Unported Licence.

In the nanocomposite, the anisotropic growth of the Ag NWs was found dependent on the molecular weight of PVP, on the $AgNO_3$ : PVP molar ratio, injection mode of the His-RGO complex and on its dissociation state. Neat Ag NWs have been effectively synthesized using PVP at the $M_w$ of 55 kDa,[18] but in presence of His-RGO, such a low $M_w$ was found ineffective in assisting and promoting the anisotropic growth of the NWs (Fig. S7b and c), likely due to i. competition of the functionalities of His grafted on the sheets in coordinating the Ag NWs surface in growth, and ii. steric hindrance of His-RGO, that limits Ag atom monomers diffusion in solution, resulting mostly in spherical and micrometre sized Ag nanostructures.

7. *Ostwald ripening*: at the seventh $AgNO_3$ injection, smaller Ag NPs (Fig. 7, step III) which possess high surface energy due to their surface to volume ratio, begin to dissolve *via* Ostwald ripening.[31]

The released Ag atoms preferentially deposit onto the energetically favourable {111} facets of pentagonal twinned seeds (Fig. 7, step III) feeding their anisotropic growth (Fig. 7, steps IV).[31] This process induces the formation of Ag filaments, which continue to elongate uniaxially as new Ag monomers are incorporated.

Upon addition of the His-RGO complex, the preformed Ag nodules or filaments bind by coordination to the His-RGO basal plane (Fig. 7, step V), initiating the *in situ* NWs growth and in the following additions, the size of the Ag NPs increases due to Ostwald ripening phenomena, as well as that of the NWs (Fig. 7, step VI).

It worth noticing that, for reaction times between 5 h and 6.5 h, the monodispersion of the Ag NWs within the nanocomposite improved without the need for size separation, temperature adjustment, precipitation and solvent redispersion steps, reflux or further addition of PVP.[49] To the best of our knowledge, this effect has not been yet discussed in the literature for graphene–Ag NWs nanocomposite and can be reasonably attributed to the size focusing phenomenon (Fig. 7, step VI).[54]

These results suggest that, at the investigated temperature, PVP ligand preferentially coordinates to defect sites on the Ag NWs – which have higher chemical reactivity due to twinning boundaries, associated with increased stress and lower lattice stabilization energy. This selective coordination facilitates the dynamic exchange and transport of coordinated clusters or atoms from the longer, thicker NWs (which dissolve into the solvent) to the shorter, thinner ones. As a result, the system gradually approaches an equilibrium between etching and redeposition processes, ultimately leading to size focusing and the formation of monodisperse NWs (Fig. 7, step VI).

# Experimental section

### Materials

Reduced Graphene Oxide (RGO, 1.6 nm flakes) was purchased from Graphene Supermarket, polyvinylpyrrolidone (PVP) (monomer based calculation, $M_w$ = 55 kDa and 360 kDa), NaCl (>99.8%), silver nitrate ($AgNO_3$, 99.9999%), acetone (99.9%), ethanol (>99.9%), 1-octadecene (ODE), DL-histidine (His, >99%) and 1,2-ethandiol (EG, >99%, Honeywell) were purchased from Sigma Aldrich.

### Exfoliation and functionalization of RGO with histidine (His)

Exfoliation and functionalization of RGO with His were performed by sonication of a dispersion, 100 mg $mL^{-1}$ in RGO and 160 mg $mL^{-1}$ in His, in Milli-Q water at pH 11.[20,21] The dispersion was sonicated for 8 h to allow exfoliation and functionalization of the RGO sheets with His, and it was purified from the excess of His by three cycles of centrifugation (40 000 rpm, 30 min) and re-dispersion in Milli-Q water. After the third centrifugation, the His-RGO pellet was re-dispersed in Milli-Q water, at both pH 7 and pH 11, and was finally isolated by centrifugation (40 000 rpm, 30 min) and dried at 70 °C in an oven.

### Synthesis of Ag NWs

Ag NWs were synthesized by the polyol synthesis approach reported by S. Coskun *et al.*[18] In a typical experiment, a vial filled up with a solution of 250 mg of PVP ($M_w$ = 360 kDa) and 3.5 mg of NaCl in 5 mL of EG, closed with a septum, was heated to 170 °C by immersion in an oil bath placed onto a hotplate, and stirred at 600 rpm. To this solution, ten injections of 0.25 mL of a 20 mg $mL^{-1}$ $AgNO_3$ solution in EG, were added, every 6 min, by a syringe. At the end of the injections, the vial was allowed to stir at 600 rpm and at 170 °C for 90 min, and then, was air-cooled down to room temperature, to stop the reaction. The NWs were purified from the excess of PVP and EG by three cycles of centrifugation (10 000 rpm, 30 min) with acetone and re-dispersion in ethanol and were finally dispersed in ethanol.

### Synthesis of hybrid nanocomposites formed of His functionalized RGO decorated with Ag NWs

The hybrid nanocomposites formed of His-RGO decorated with Ag NWs (His-RGO/Ag NWs) were synthesized modifying the polyol synthesis approach of Ag NWs,[18] by injecting the His-RGO complex in the synthesis solution of the Ag NWs.

A first experiment involved introducing 2.5 mL of a 20 mg $mL^{-1}$ $AgNO_3$ in EG through ten 0.25 mL injections, spaced 6 min apart into a mixture comprising 250 mg of PVP, 3.5 mg of NaCl, and 5 mg of His-RGO, in 5 mL of EG. The reaction setup was a vial sealed with a septum, heated up to 170 °C onto a hotplate by using an oil bath, and stirred at 600 rpm. Following the completion of the ten $AgNO_3$ injections, the vial continued to be stirred at 170 °C and 600 rpm for 90 min. Subsequently, the reaction was quenched by allowing the vial to air-cool down to room temperature.

In a second experiment, a dispersion containing 5 mg of His-RGO in 2 mL of EG pre-heated up to 170 °C was injected into a mixture containing 250 mg of PVP, 3.5 mg of NaCl, and 5 mg of His-RGO in 5 mL of EG, at the conclusion of the ten 2.5 mL injections of a 20 mg $mL^{-1}$ $AgNO_3$ in EG. This composite was contained in a vial sealed with a septum, heated up to

Open Access Article. Published on 18 February 2026. Downloaded on 3/17/2026 3:37:48 PM.
This article is licensed under a Creative Commons Attribution-NonCommercial 3.0 Unported Licence.

170 °C using an oil bath, and stirred at 600 rpm. Following the completion of the $AgNO_3$ injections, the vial continued to be stirred at 600 rpm and 170 °C for 90 min, after which it was air-cooled to room temperature.

A third set of experiments was conducted by injecting a dispersion of His-RGO in 2 mL of pre-heated (170 °C) EG, into the synthesis solution containing PVP and 3.5 mg of NaCl in 5 mL of EG. This mixture was placed in a vial sealed with a septum, heated up to 170 °C onto a hotplate *via* immersion in an oil bath, and subjected to stirring. The injection occurred between the seventh and eighth of the ten 0.25 mL injections of the 2.5 mL 20 mg $mL^{-1}$ $AgNO_3$ solution in EG. Subsequently, the vial was air-cooled down to room temperature. In this series of experiments, variations were introduced, including 5 mg and 10 mg of His-RGO in 2 mL of EG (with His-RGO powder isolated from Milli-Q water solutions at pH 7 and pH 11 having ζ-potential of −20.1 ± 1.5 mV and −24.5 ± 1.8 mV, respectively), 250 mg and 375 mg of PVP (at molecular weights of 55 kDa and 360 kDa), reaction times of 1.5 h, 2.5 h, 6.5 h, and 7.5 h, and stirring rates of both 600 rpm and 200 rpm.

Following the syntheses, the obtained hybrid nanocomposites underwent purification from excess PVP and EG through six cycles of centrifugation with acetone (10 000 rpm, 10 min) and subsequent re-dispersion in ethanol. The resulting hybrid nanocomposites were then re-dispersed in ethanol.

### Characterization techniques

Steady state UV-Vis absorption spectroscopy investigation was performed by a Cary Varian 5000 spectrophotometer at room temperature.

Surface charge of the His-RGO complex was determined by ζ-potential measurements carried out by laser Doppler velocimetry method, after sample dilution in Milli-Q water. Data were reported as mean values ± standard deviation of three independent experiments.

Raman spectra were collected by using a LabRAM HR Horiba-Jobin Yvon spectrometer with a 532 nm continuous excitation laser source. Measurements were carried out under ambient conditions at a low laser power (1 mW) to avoid laser-induced damage of the sample. The Raman signal from the silicon wafer at 520 $cm^{-1}$ was used to calibrate the spectrometer and accuracy of the spectral measurement was 1 $cm^{-1}$.

Mid-infrared spectra were acquired by a Varian 670-IR spectrometer equipped with a DTGS (Deuterated Tryglycine Sulfate) detector having a spectral resolution of 4 $cm^{-1}$. For attenuated total reflection (ATR) measurements, a one-bounce 2 mm diameter diamond microprism was used as internal reflection element (IRE). The samples were deposited by drop casting directly onto the upper face of the diamond crystal and the solvent was allowed to evaporate.

Transmission Electron Microscopy (TEM) images were collected by a JEOL JEM-1011 microscope working at an accelerating voltage of 100 kV, equipped by a high-contrast objective lens and a W filament as electron source. Under these conditions, the ultimate point resolution of the microscope was 0.34 nm. The TEM images were recorded by a Gatan SC-1000 Orius Camera, equipped with a fiber-optical coupled 11 Mp CCD. The samples were prepared by dipping a 300 mesh amorphous carbon-coated Cu grid in ethanol dispersions of neat Ag NWs and of His-RGO/Ag NWs, then letting the solvent to evaporate. Size statistical analyses of the NWs average length and diameter were performed by the freeware Image J analysis program.

## Conclusions

In this work, we have demonstrated a novel polyol-based strategy for the synthesis of a hybrid nanocomposite consisting of histidine functionalized RGO (His-RGO) sheets, decorated with polyvinylpyrrolidone (PVP)-stabilized Ag NWs. Unlike conventional post-synthetic mixing approaches, which often result in a weak interfacial coupling, this method enables anisotropic growth of Ag NWs on His-RGO, yielding a hybrid material with stronger interfacial interactions.

A central advance lies in the multifunctional role of histidine (His). His promotes the exfoliation and stable dispersion of RGO in water, eliminating the need for toxic, high-boiling organic solvents. At the same time, it ensures compatibility with ethylene glycol (EG), which here acts simultaneously as a green solvent and reducing agent, further reinforcing the sustainability of the synthesis.

Mechanistic investigations revealed that the controlled injection of $AgNO_3$ into a PVP/NaCl/EG solution leads to the formation of AgCl nanocubes, which act as reservoirs of $Ag^+$ ions. These ions were slowly released and reduced by EG on the nanocube surfaces to generate Ag nodules and spherical nanoparticles (NPs). Upon addition of His-RGO, the carboxyl, amino and imidazole groups of His coordinated the nodules, creating heterogeneous nucleation sites that drove the evolution of seeds into Ag filaments and, ultimately, NWs. The anisotropic growth is sustained by Ostwald ripening, where smaller Ag NPs dissolve and feed the elongation of the filaments. In parallel, the selective passivation of {100} facets by PVP and size focusing effects ensure thermodynamic control and promote NW monodispersion.

By tuning key parameters, including the His-RGO dissociation state, $AgNO_3$ : His-RGO w/w, PVP molecular weight, PVP : $AgNO_3$ molar ratio, stirring rate, and reaction time, we obtained His-RGO sheets decorated with uniform, monodisperse Ag NWs (2.8 ± 0.8 μm in length and 50 ± 10 nm in thickness). This tunability provides both a mechanistic framework and a scalable synthetic route for graphene–metal hybrids and potentially other inorganic nanostructures.

The resulting His-RGO/Ag NW nanocomposite represents a highly versatile and robust material platform with significant potential across multiple technological domains, including electrochemical (bio)sensors, flexible and wearable electronics, UV-protective coatings, and thermal management. The direct anchoring of Ag NWs onto the RGO basal plane *via* His establishes intimate interfacial contact and promotes strong elec-


This journal is © The Royal Society of Chemistry 2026

Open Access Article. Published on 18 February 2026. Downloaded on 3/17/2026 3:37:48 PM. This article is licensed under a Creative Commons Attribution-NonCommercial 3.0 Unported Licence.

tronic coupling, with the molecular linker acting as a charge-transport channel between the two components, with the molecular linker acting as a charge-transport bridge between the two components. This architecture also creates continuous conductive pathways that are expected to reduce interfacial resistance and facilitate the dissipation of heat and photo-induced energy. Moreover, the anchored configuration can limit nanowire aggregation and could contribute to improved chemical stability under thermal stress or prolonged UV exposure, although dedicated durability studies are required to quantitatively confirm this effect. The presence of PVP on the Ag NW surface further enhances dispersion stability in both aqueous and alcoholic media, enabling solution-based processing for homogeneous film deposition, scalable device fabrication, textile functionalization, and reliable integration into functional systems. Collectively, these structural and chemical features are anticipated to confer improved oxidation and aggregation resistance, superior electrical conductivity, high electrochemical activity, and operational reliability. Accordingly, compared with conventional RGO–Ag NW systems, this nanocomposite is expected to provide advantages in electrochemical sensing, such as faster charge transfer and improved redox reversibility – while also supporting the scalable development of flexible, and reproducible electronic devices, UV-coatings and components for thermal management. As such, this work not only advances the controlled synthesis of hybrid nanomaterials but also lays the foundation for next-generation green technologies with high societal and industrial relevance.

## Author contributions

A. Massaro, R. A. Lakho, A. Grandolfo, G. V. Bianco: data curation, methodology. E. Fanizza, M. L. Curri, C. Ingrosso: supervision, data curation, conceptualization, writing – original draft, writing – review and editing. C. Ingrosso, M. L. Curri, E. Fanizza, R. Comparelli, M. Striccoli: funding acquisition and reviewing.

## Conflicts of interest

There are no conflicts to declare.

## Data availability

The data supporting the findings of this study are available within the article and its supplementary information (SI). TEM images of nanostructures isolated by centrifugation from the synthesis solution of Ag NWs; TEM images of His-RGO/Ag NWs synthesized under different investigated experimental conditions; Histograms of the lengths and diameters distribution of Ag NWs in His-RGO/Ag NWs; TEM iamges of His-RGO/Ag NWs purified with acetone and treated with a concentrated ammonia/30% hydrogen peroxide solution; Raman spectrum of His-RGO/Ag NWs; ATR-FTIR spectra of PVP and His-RGO/Ag NWs. Supplementary information is available. See DOI: https://doi.org/10.1039/d5nr04827c.

## Acknowledgements

This publication was made possible thanks to the ZEROIMPACT Project funded under the bilateral agreement CNR/MHESR (Italy, Tunisia) (biennium 2025–2026), and IDEA Project funded under the bilateral agreement CNR-CNPq (Italy, Brazil) (biennium 2025–2026).

## References

1 I. Sadiq, S. A. Ali and T. Ahmad, *ACS Appl. Energy Mater.*, 2025, **8**, 5544–5563.
2 T. L. Phan, T. T. Le, V. D. Doan, H. A. V. Truong and V. T. Le, *Inorg. Chem. Commun.*, 2025, **180**, 114934.
3 C. Ingrosso, M. Corricelli, A. Testolin, V. Pifferi, F. Bettazzi, G. V. Bianco, N. Depalo, E. Fanizza, M. Striccoli, I. Palchetti, M. L. Curri and L. Falciola, *Mater. Adv.*, 2024, **5**, 549–560.
4 F. Vischio, L. Carrieri, G. V. Bianco, F. Petronella, N. Depalo, E. Fanizza, M. P. Scavo, L. De Sio, A. Calogero and M. Striccoli, *Biomater. Adv.*, 2023, **145**, 213272.
5 B. Verma, A. Kumar, H. C. Swart and V. Kumar, *Chem. Inorg. Mater.*, 2025, **5**, 100097.
6 C. Ingrosso, A. Petrella, M. L. Curri, M. Striccoli, P. Cosma, P. D. Cozzoli and A. Agostiano, *Appl. Surf. Sci.*, 2005, **246**, 367–371.
7 V. Georgakilas, J. N. Tiwari, K. C. Kemp, J. A. Perman, A. B. Bourlinos, K. S. Kim and R. Zboril, *Chem. Rev.*, 2016, **116**, 5464–5519.
8 D. A. Dinh, K. S. Hui, K. N. Hui, Y. R. Cho, W. Zhou, X. Hong and H.-H. Chun, *Appl. Surf. Sci.*, 2014, **298**, 62–67.
9 X. Wang, S. Liu, W. Kang, Y. Zhang and H. Kou, *AIP Adv.*, 2025, **15**, 015311.
10 M. Cao, M. Wang, L. Li, H. Qiu, M. A. Padhiar and Z. Yang, *Nano Energy*, 2018, **50**, 528–535.
11 A. Baranowska-Korczyc, D. Kowalczyk, M. Chodkowski, M. Krzyżowska and M. Cieślak, *Mater. Today Commun.*, 2025, **48**, 113589.
12 Z. Chen, Y. Liu, W. Yu, S. Liu and Y. Huang, *ACS Appl. Nano Mater.*, 2025, **8**, 5602–5610.
13 S. Wu, K. S. Hui and K. N. Hui, *J. Phys. Chem. C*, 2015, **119**, 23358–23365.
14 S. Chen, H. Li, K. Zhao and D. Wu, *Sol. Energy*, 2020, **198**, 167–174.
15 H. Jia, Z.-L. Yi, X.-H. Huang, F.-Y. Su, Q.-Q. Kong, X. Yang, Z. Wang, L.-J. Xie, Q.-G. Guo and C.-M. Chen, *Carbon*, 2021, **183**, 809–819.
16 A. K. Nair, K. B. Bhavitha, S. Perumbilavil, P. Sankar, D. Rouxel, M. S. Kala, S. Thomas and N. Kalarikkal, *Carbon*, 2018, **132**, 380–393.

Open Access Article. Published on 18 February 2026. Downloaded on 3/17/2026 3:37:48 PM. This article is licensed under a Creative Commons Attribution-NonCommercial 3.0 Unported Licence.

17 N. Ahmad, N. Abdullah and F. Yasin, *Toxicol. Rep.*, 2020, **7**, 693–699.
18 S. Coskun, B. Aksoy and H. E. Unalan, *Cryst. Growth Des.*, 2011, **11**, 4963–4969.
19 J. G. Mesu, T. Visser, F. Soulimani and B. M. Weckhuysen, *Vib. Spectrosc.*, 2005, **39**, 114–125.
20 Y. Hernandez, V. Nicolosi, M. Lotya, F. M. Blighe, Z. Sun, S. De, I. T. McGovern, B. Holland, M. Byrne and Y. K. Gun'Ko, *Nat. Nanotechnol.*, 2008, **3**, 563–568.
21 S. Elumalai, S. B. Jaber, S. Chandrasekaran and M. Ogawa, *Phys. Chem. Chem. Phys.*, 2020, **22**, 9910–9914.
22 L. Zhang, Y. Sheng, A. Z. Yazdi, K. Sarikhani, F. Wang, Y. Jiang, J. Liu, T. Zheng, W. Wang, P. Ouyang and P. Chen, *Nanoscale*, 2019, **11**, 2999–3012.
23 C. K. Chua and M. Pumera, *Chem. Soc. Rev.*, 2014, **43**, 291–312.
24 G. Mandriota, A. Grandolfo, R. Striani, A. Panniello, G. V. Bianco, A. Milella, C. Mele, R. Comparelli, A. Greco and M. Striccoli, *Appl. Surf. Sci.*, 2025, **684**, 161884.
25 A. Grandolfo, I. De Pasquale, G. Mandriota, A. Milella, M. P. Scavo, M. De Luca, F. Balestra, G. Panzetta, S. Bettini, F. Rizzi, R. Comparelli, E. Fanizza, M. Striccoli, M. L. Curri and C. Ingrosso, *Carbon*, 2026, **246**, 120902.
26 A. C. Ferrari, *Solid State Commun.*, 2007, **143**, 47–57.
27 A. C. Ferrari and J. Robertson, *Phys. Rev. B:Condens. Matter Mater. Phys.*, 2000, **61**, 14095–14107.
28 W. M. Schuette and W. E. Buhro, *ACS Nano*, 2013, **7**, 3844–3853.
29 T. Efimova, M. Khombak, A. Ramanenka, P. Kratovich and O. Kulakovich, *Plasmonics*, 2025, **20**, 6213–6220.
30 R. Dong, B. Tian, C. Zeng, T. Li, T. Wang and J. Zhang, *J. Phys. Chem. C*, 2012, **117**, 213–220.
31 S. E. Skrabalak, B. J. Wiley, M. Kim, E. V. Formo and Y. Xia, *Nano Lett.*, 2008, **8**, 2077–2081.
32 M. R. Azani and A. Hassanpour, *ChemistrySelect*, 2019, **4**, 2716–2720.
33 Y. Liu, C.-H. Liu, T. Debnath, Y. Wang, D. Pohl, L. V. Besteiro, D. M. Meira, S. Huang, F. Yang, B. Rellinghaus, M. Chaker, D. F. Perepichka and D. Ma, *Nat. Commun.*, 2023, **14**, 541.
34 M. Chen, I. Y. Phang, M. R. Lee, J. K. W. Yang and X. Y. Ling, *Langmuir*, 2013, **29**, 7061–7069.
35 S. M. Bergin, Y.-H. Chen, A. R. Rathmell, P. Charbonneau, Z.-Y. Li and B. J. Wiley, *Nanoscale*, 2012, **4**, 1996.
36 M. S. Goh, Y. H. Lee, S. Pedireddy, I. Y. Phang, W. W. Tjiu, J. M. R. Tan and X. Y. Ling, *Langmuir*, 2012, **28**, 14441–14449.
37 C. Xu, R.-s. Yuan and X. Wang, *New Carbon Mater.*, 2014, **29**, 61–66.
38 H. Alam and S. Ramakrishna, *Nano Energy*, 2013, **2**, 190–212.
39 Y.-J. Song, M. Wang, X.-Y. Zhang, J.-Y. Wu and T. Zhang, *Nanoscale Res. Lett.*, 2014, **9**, 17.
40 J. Tang, H. Sun, X. Li, F. Liang and T. Jiang, *Colloids Surf., A*, 2021, **630**, 127521.
41 Y. Sun, B. Mayers, T. Herricks and Y. Xia, *Nano Lett.*, 2003, **3**, 955–960.
42 Y.-Y. Yu, S.-S. Chang, C.-L. Lee and C. R. C. Wang, *J. Phys. Chem. B*, 1997, **101**, 6661–6664.
43 S. Link, M. B. Mohamed and M. A. El-Sayed, *J. Phys. Chem. B*, 1999, **103**, 3073–3077.
44 N. R. Jana, L. Gearheart and C. J. Murphy, *J. Phys. Chem. B*, 2001, **105**, 4065–4067.
45 C. J. Johnson, E. Dujardin, S. A. Davis, C. J. Murphy and S. Mann, *J. Mater. Chem.*, 2002, **12**, 1765–1770.
46 P. L. Gai and M. A. Harmer, *Nano Lett.*, 2002, **2**, 771–774.
47 P.-Y. Silvert, R. Herrera-Urbina and K. Tekaia-Elhsissen, *J. Mater. Chem.*, 1997, **7**, 293–299.
48 K. E. Korte, S. E. Skrabalak and Y. Xia, *J. Mater. Chem.*, 2008, **18**, 437–441.
49 J. R. Shimpi, D. S. Sidhaye and B. L. V. Prasad, *Langmuir*, 2017, **33**, 9491–9507.
50 L. D. Marks, *Rep. Prog. Phys.*, 1994, **57**, 603.
51 J. Jiu, T. Araki, J. Wang, M. Nogi, T. Sugahara, S. Nagao, H. Koga, K. Suganuma, E. Nakazawa, M. Hara, H. Uchida and K. Shinozaki, *J. Mater. Chem. A*, 2014, **2**, 6326–6330.
52 B. Wiley, Y. Sun and Y. Xia, *Acc. Chem. Res.*, 2007, **40**, 1067–1076.
53 Y. Sun and Y. Xia, *Adv. Mater.*, 2002, **14**, 833.
54 S. Mozaffari, W. Li, M. Dixit, S. Seifert, B. Lee, L. Kovarik, G. Mpourmpakis and A. M. Karim, *Nanoscale Adv.*, 2019, **1**, 4052–4066.


This journal is © The Royal Society of Chemistry 2026